

Three-Dimensional Si Anodes with Fast Diffusion, High Capacity, High Rate Capability, and Long Cycle Life

Shailendra Chiluwal, Nawraj Sapkota, Apparao M. Rao, and Ramakrishna Podila*



Cite This: *ACS Appl. Mater. Interfaces* 2020, 12, 34763–34770



Read Online

ACCESS |

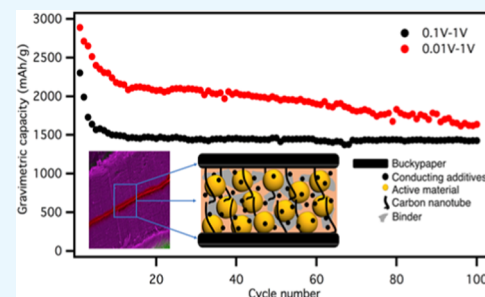
Metrics & More

Article Recommendations

Supporting Information

ABSTRACT: There are many interfaces in conventional nanostructured silicon anodes for LIBs, including (1) the solid–electrolyte interface (SEI), (2) interfaces between Si nanoparticles (NPs) and binders, and (3) interface between the current collector and active materials (CCAMI). Interfacial layers (e.g., graphene, activated carbon) coated on conventional Cu foil current collectors are often used to improve charge transfer and reduce CCAMI resistance. Indeed, our detailed studies show that the introduction of interfacial graphene layers results in an ~20–60% increase in capacity after 500 cycles at 0.1 C. While the capacity is enhanced by inclusion of interfacial layers or conductive additives, they do not resolve problems associated with the diffusion of Li^+ ions in the anode. Such electrodes that cannot accommodate the fast diffusion of Li^+ ions are prone to plating. Here, we show that the use of freestanding and scalably produced carbon nanotube (CNT) Bucky paper or Bucky sandwich electrodes containing Si NPs (diameter of ~100 nm) exhibits up to ~1200 and 1900% increases in the gravimetric capacity after 500 cycles at 0.1 C, respectively, when discharged to 0.1 V. Using detailed electrochemical impedance spectroscopy, we show that the diffusion time constants in the Bucky paper and Bucky sandwich electrodes are increased by 2 orders of magnitude compared to that in the bare Cu foil. Furthermore, we demonstrate that the Bucky paper and Bucky sandwich electrodes can withstand high rates up to 4 C and show long cycle life up to ~500 cycles at 0.1 C. Finally, we show that the Bucky sandwich electrode architecture with smaller diameter Si NPs (~30 nm) leads to capacities as high as ~1490 mAh/g (~1635 mAh/g) at 0.1 C up to 100 cycles when discharged to 0.1 V (0.01 V).

KEYWORDS: silicon anode, Bucky paper, three-dimensional current collector, Li-ion battery, electrochemical impedance spectroscopy, fast diffusion



INTRODUCTION

The U.S. Advanced Battery Consortium (USABC) goals for low-cost electric vehicle (EV) batteries by 2023 is 15 min charging for 80% of the pack capacity, along with other key metrics (US\$75 kWh⁻¹, 550 Wh/L, and 275 Wh/kg at the cell level).¹ To achieve these goals, it is imperative to redesign the conventional Li-ion battery (LIB) electrode composition and configuration by using both new materials and novel architectures for better cathodes (e.g., sulfur) and anodes (e.g., silicon). Graphitic anodes initially enabled LIBs to become commercially viable and are still used widely due to their low cost and excellent stability. Different forms of carbon, such as graphite, carbon nanotubes (CNTs), carbon fibers, exfoliated graphene, reduced graphene oxide, etc., have also been used as anodes albeit with incremental improvement in battery capacity.² The close proximity of the graphene-based material's potential to that of Li^+/Li^0 makes carbon anodes particularly susceptible to Li plating. Therefore, anode chemistries with safer working voltages are attractive for fast-charging batteries.¹ Beyond graphite anodes, titanium-based oxides (e.g., lithium titanate or LTO) also have received much attention because they show a low volume change (2–3%)

upon Li insertion/de-insertion, in addition to exhibiting an excellent cycling life.^{3–6} Despite their advantages, intercalating anodes based on carbon and LTO have limited theoretical capacities of ~375 and ~600 mAh/g, respectively. Alternatively, many conversion/alloying anodes have emerged and are poised to displace existing intercalation anodes.⁷

Although many conversion/alloying anodes are available, Si anodes have received much attention because Si has both the highest gravimetric capacity (4200 mAh/g, $\text{Li}_{22}\text{Si}_5$) and volumetric capacity (9786 mAh/cm³). Such a high specific capacity arises from the formation of intermetallic Li–Si binary compounds, such as $\text{Li}_{12}\text{Si}_7$, Li_7Si_3 , $\text{Li}_{13}\text{Si}_4$, and $\text{Li}_{22}\text{Si}_5$. However, the practical application of Si anodes has been impeded by the lower electrical conductivity of Si, large volume expansion upon lithiation (~400%) during first

Received: April 1, 2020

Accepted: July 8, 2020

Published: July 8, 2020



discharge, and pulverization during subsequent cycling.^{8–10} Additionally, phase changes that occur during cycling of Si anodes lead to a decrease in the specific capacity during the first irreversible cycle.^{10,11}

In the recent past, much research has focused on using Si nanostructures (e.g., Si nanoparticles or Si NPs) because of their ability to resist mechanical degradation at the particle and/or electrode level. As discussed in ref 12, many studies investigated the mechanism of stress generation, cracking, and fracture of silicon (which is dependent on the size of Si) using numerical calculations,¹³ scanning electron microscopy (SEM),¹⁴ and transmission electron microscopy (TEM).¹⁵ Based on these studies, the critical fracture sizes of crystalline Si nanostructures were identified to be \sim 150–400 nm depending on the electrochemical reaction rate.¹⁶ Liu et al.¹⁶ reported that the size of Si NPs is strongly related to cracking. They observed cracking in individual NPs only above 150 nm. Smaller sized NPs have higher stress-to-strain tolerance, which prevents pulverization. Aghajamali et al.¹⁷ also reported the size-dependent effect by using the Si NPs of 3, 5, 8, and 15 nm. They were able to achieve 500 stable cycles with a 1000 mAh/g specific capacity. More interestingly, they found that \sim 3 nm Si NPs were more stable compared to the 15 nm, which again highlights the importance of nanosizing to improve the performance of Si anodes. In addition to nanostructuring, Si NPs have also been mixed/attached with a conducting polymer/binder or coated/mixed with some form of carbon (graphene/CNT/graphene oxide matrix) to achieve better performance by improving electrical conductivity at the electrode level.^{8,18–24}

Despite these improvements at the active material (AM) level, two important challenges still remain with regard to Si electrode configuration: (1) reducing the interfacial resistance between the current collector (CC) and AM (i.e., CC–AM interface or CCAMI) consistently over hundreds of cycles with new electrode architectures to achieve better performance. In the case of Si anodes, Si AM particles (even if they are impervious to pulverization) fuse into each other due to volume expansion during lithiation, leading to cracks and electrically disconnected regions within the AM layer over a few cycles, which could eventually result in physical delamination. Electrode architectures that facilitate low CCAMI by accommodating crack formation and delamination are necessary for achieving electrodes with long cyclability and (2) designing electrode architectures that facilitate fast diffusion of Li⁺ in and out of a reaction site while mitigating Li⁺ plating on the electrode surface. In an electrode limited by diffusion, only a certain amount of Li⁺ can enter the active material per unit time at a given temperature. Following initial lithiation of AM, the rate at which more Li⁺ can enter decreases. This effect is highly pronounced if the diffusion impedance is high. If Li⁺ transport to the surface of the electrode is faster than the rate that AM can react with Li⁺, Li can plate on the surface of the electrode and eventually lead to cell failure. Finally, the electrode architecture should ideally lead to low diffusion time constants to improve the overall capacity. These challenges are later referred to as challenges 1 and 2 in the article.

We previously showed that a simple CCAMI layer (viz., a few micron thick layer of sp²-activated carbon or of CNTs on Al) plays a very critical role in improving the cathode electrochemical performance (especially high charge rates up to 4 C) in accordance with USABC goals.^{25,26} Additionally,

some previous articles have reported an improvement in the CCAMI by applying an interfacial layer of carbon materials.^{27–32} Nevertheless, such electrodes do not address diffusion issues (i.e., mitigating the possibility of Li⁺ plating) and are still limited to a laminated structure of conventional batteries that restricts the ion transport between electrodes to be only one-dimensional in nature. While the concept of extending battery architecture into three dimensions has been proposed for more than a decade,¹ large-scale three-dimensional (3D) electrodes that simultaneously alleviate CCAMI and diffusion issues have not yet been realized.

In this article, we show that it is necessary to address the above two challenges simultaneously to improve battery performance. To this end, using 100 nm Si NPs, we prepared (a) electrodes with an interfacial layer (activated carbon represented as C and graphene) that address CCAMI (Cu/Si NPs (bare Cu), Cu/C/Si NPs (Cu/C), and Cu/graphene/Si NPs (Cu/graphene)), (b) electrodes that use an ion-permeable CNT Bucky paper or BP as the current collector (BP/Si NPs or Bucky; Figure S1), and (c) quasi-3D electrodes with Si NPs sandwiched between two freestanding BPs (BP/Si NPs/BP or Bucky sandwich). All of the electrodes were prepared using traditional coating techniques that are amenable for scalable production (see the **Supporting Information** for a detailed discussion of materials and methods). The incorporation of an interfacial layer in (a) viz., Cu/C and Cu/graphene electrodes led to an \sim 20–60% enhancement in the gravimetric capacity relative to bare Cu due to a reduction in the CCAMI resistance. In (b), we alleviated the need for the traditional Cu current collector and addressed the diffusion impedance issue by using an entangled quasi-two-dimensional (2D) CNT BP, which led to an \sim 1200% increase in capacity. Given that CNTs are permeable to Li⁺ ions, we used two BPs to achieve a sandwich structure encapsulating Si NPs in (c) to address the CCAMI and diffusion impedance issue simultaneously. This was found to result in an \sim 1900% increase in capacity. We analyzed the changes in the electrochemical processes in different electrodes using detailed electrochemical impedance spectroscopy (EIS) studies. Our EIS studies showed that Bucky sandwich electrodes significantly reduce Warburg impedance and CCAMI resistance. Consequently, we found that Bucky sandwich outperforms both Si NPs/BP and Si NPs/Cu/C or Cu/graphene electrodes with a capacity as high as \sim 500 mAh/g after 500 cycles at 0.1 C for 100 nm particles and up to \sim 1490 mAh/g after 100 cycles at 0.1 C for 30 nm Si NPs when discharged to 0.1 V. Furthermore, we found that Bucky and Bucky sandwich electrodes are stable even at rates as high as 4 C.

RESULTS AND DISCUSSION

Traditionally, CCAMI is addressed by coating an sp²-activated carbon layer on Cu foil prior to coating the AM slurry containing AM, binder, and conducting additives. Similarly, graphene has also been used as a thin CCAMI layer to improve the interface between Cu and AM.³³ However, as detailed in the following discussion, these interfacial layers only lead to incremental improvements as they do not address issues of a 3D contact between CC and Si NPs (challenge 1) or Li⁺ ion diffusion in the electrode by having a current collector that is permeable to Li⁺ (challenge 2).

As shown in the electron micrographs in Figure 1a–c, Si NPs adhered well to all of the substrates upon coating. Unlike

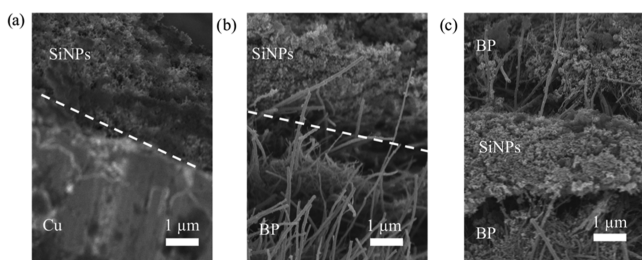


Figure 1. Scanning electron micrographs of different electrodes: (a) a traditional Si NP anode coated on Cu foil, (b) an electrode prepared similar to (a) by replacing Cu foil with a lightweight randomly entangled freestanding network of CNTs known as Bucky paper (BP), (c) Si NPs are coated on a first BP and then sandwiched with a second BP layer to provide a three-dimensional architecture. All of the electrodes are prepared using the standard conventional coating and drying processes used in Li-ion battery manufacturing.

the Cu current collector in samples (bare Cu, Cu/C, Cu/graphene), Si NPs are more uniformly in contact with CNTs in samples Bucky and Bucky sandwich due to the porosity and flexibility of the BP, inherently tubular nature of CNTs, and their high specific surface area compared to Cu electrodes. It should be noted that elemental maps of Bucky sandwich, Si NPs/BP, and Si NP/Cu electrodes are discussed later in Figures 6–8. It should be noted that the SEM images for samples (bare Cu, Cu/C, Cu/graphene) look similar as the interfacial layer is very thin (<100 nm). More importantly, in samples (Cu/C, Cu/graphene), the Cu surface or the interfacial layer (activated carbon or graphene) is directly in contact with only the bottom-most layer of the coated Si NPs. However, the AM layer containing Si NPs/conductive additives/binder is $\sim 36 \mu\text{m}$ in all of the samples. Thus, as shown in Figure 2a, only the bottom-most layer of Si NP particles within the AM layer is in direct contact with either the interfacial layer or the Cu foil. However, in the case of BP-based electrodes (viz., Bucky and Bucky sandwich), the contact between the current collector and Si NPs is not limited to the bottom-most layer but is more uniform throughout the electrode, particularly in the case of Bucky sandwich (Figure 2b). More importantly, different Si NPs within the AM layer fuse due to volume expansion of Si upon lithiation. Thus, large cracks often develop within the electrode over a few cycles. As

discussed later, Bucky and Bucky sandwich electrodes facilitate excellent electrical connection even in the presence of large cracks within the AM layer.

Although it is known that Si NPs (<150 nm) are more resistant to pulverization, electrodes that do not address CCAMI are not useful for long cycling at high charge rates. In the case of Cu-based electrodes (viz., bare Cu, Cu/C, Cu/graphene), the CCAMI resistance across the plane is very high because interfacial layers such as graphene or activated carbon are only good in-plane conductors. On the other hand, samples Bucky and Bucky sandwich provide a more uniform electrical contact with Si NPs alleviating the issues with possible delamination. Furthermore, as shown in Figure 2b, even if the AM layer delaminates at higher rates, the Bucky sandwich is capable of containing the AM within the electrode without significantly affecting the performance.

To understand the changes in charge-transfer resistance in electrodes used in this study, we performed extensive EIS studies to understand the influence of CCAMI resistance in laminated Cu electrodes and BP/sandwich electrodes (Figures 3, S2, and S3). In a typical EIS experiment, a small sinusoidal ac voltage of fixed frequency (scanned from milliHertz to several megaHertz) is applied to an electrochemical cell and the ensuing current is measured. A typical battery EIS response is shown in Figure 3a with high- and low-frequency regions. As shown in Figure 3a–c, EIS responses of all of the electrodes showed a semicircle in the high-frequency region, while a line was observed in the low-frequency region. Traditionally, EIS responses are fit to a circuit that consists of a bulk electrolyte resistance (R_o), a charge-transfer resistance (R_{ct}), a double layer capacitance (C_{dl}) of the electrode–electrolyte interface, and a Warburg impedance (Z_W) arising from the diffusion of the electroactive species. A resistor R_s and a capacitor C_s , connected in parallel, are often added to the circuit to take into account the formation of surface film at the electrode surface. Such traditional circuits that are often used for battery electrodes did not yield good fits to our data. In such cases, a constant-phase element (CPE) is often used to improve the fit based on an assertion that the distribution of time constants is present in the system under investigation.³⁴ In our case, good fits were obtained by using CPEs Q_s and Q_{ct} (Figure S4). Although the use of CPE can provide some relevant information about frequency-independent charge-transfer

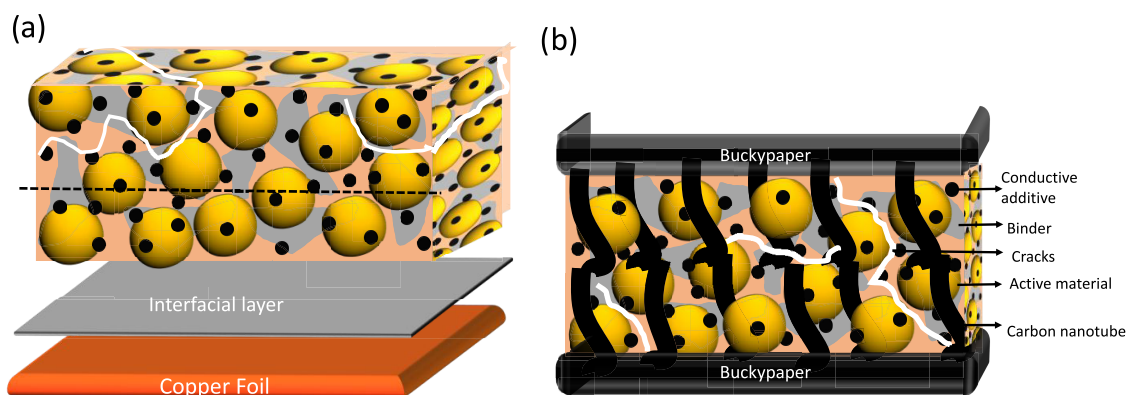


Figure 2. (a, b) Schematic representations of Cu-based and BP-based electrodes, respectively. While only the bottom-most layer of Si NPs (below the dashed line in (a)) is in direct contact with either the interfacial layer or Cu foil surface, there are more uniformly distributed electrical and thermal contacts in the BP-based electrodes. Thus, even in the presence of large cracks (shown in white), the BP-based electrodes maintain excellent electrical connection.

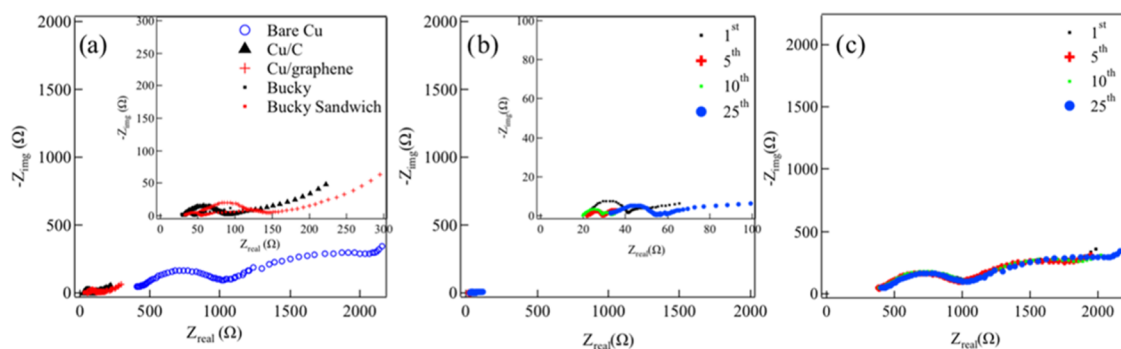


Figure 3. (a) EIS spectra for all electrodes at 0.1 V for the 25th cycle. The inset shows that the BP-based electrodes display a significantly lower resistance (~ 20 – 30 Ω) unlike bare Cu (~ 450 Ω). (b, c) EIS data for 1–25 cycles for BP/Si NPs/BP and bare Cu/Si NP electrodes, which suggests that the resistance does not show much change after 25 cycles for all of the electrodes. The inset in (b) shows a magnified view of EIS spectra for the BP/Si NP/BP electrode.

resistance, it does not provide any direct physical insights into time constants.³⁴ To directly understand the nature of the time constant distribution (assumed to be present for CPE fitting, as discussed later in Figure 9), we fitted the total impedance (Z) as a function of frequency. Using the CPE fits, as shown in Table S1, R_{ct} values for Bucky and Bucky sandwich electrodes (~ 21 and 25 Ω , respectively) were found to be significantly lower compared to other Cu-based electrodes after 25 cycles. Again, it is worth noting that the fits using CPE provide good estimates of frequency-independent R_{ct} values but do not describe frequency-dependent physical phenomena (e.g., diffusion impedance) completely. Although bare Cu foil showed a high R_{ct} of ~ 643 Ω , Cu/C and Cu/graphene electrodes showed much lower R_{ct} ~ 58 and ~ 73 Ω after 25 cycles, respectively. Such a decrease is expected because the presence of interfacial carbon and graphene layers reduces R_{ct} similar to BP-based electrodes. Indeed, from the standpoint of R_{ct} Bucky and Bucky sandwich electrodes were comparable to Cu/C and Cu/graphene. Although such a comparable R_{ct} suggests that the electrochemical performance of Bucky, Bucky sandwich, Cu/C, and Cu/graphene should be similar, we found that Bucky and Bucky sandwich electrodes significantly outperformed Cu/C and Cu/graphene. We attribute such a difference in performance to a faster diffusion time constant in Bucky electrodes. The diffusion time constants are discussed later in Figure 6 after highlighting the salient features of the overall electrochemical performance in Figures 4 and 5.

As shown in Figure 4a,b, we also evaluated the electrochemical performance of all of the electrodes by assembling coin cells. All of the coin cells were tested between 0.1 and 1 V to avoid the amorphous-phase transformation of Si below 0.1 V. We tested the cells under different C-rates (0.1, 0.5, 1, 2, 4, and 0.1 C) for five cycles each (Figure 4a,b). It can be clearly seen that Bucky and Bucky sandwich electrodes showed a much superior gravimetric capacity at all of the rates compared to the other electrodes. More importantly, our rate capability tests showed that Bucky and Bucky sandwich electrodes were able to withstand rates as high as 4 C. In the case of Bucky sandwich, we found an average capacity of ~ 595 mAh/g for the first 5 cycles, which could be recovered even after cycling at 4 C. The charge and discharge profiles for all electrodes are shown in the Supporting Information, Figures S5 and S6. Our cycling stability tests (Figure 4c,d) showed that the Bucky and Bucky sandwich electrodes are stable up to 500 cycles at a 0.1 C rate with up to 71% capacity retention (~ 385 and 500 mAh/g for Bucky and Bucky sandwich electrodes, respectively). In

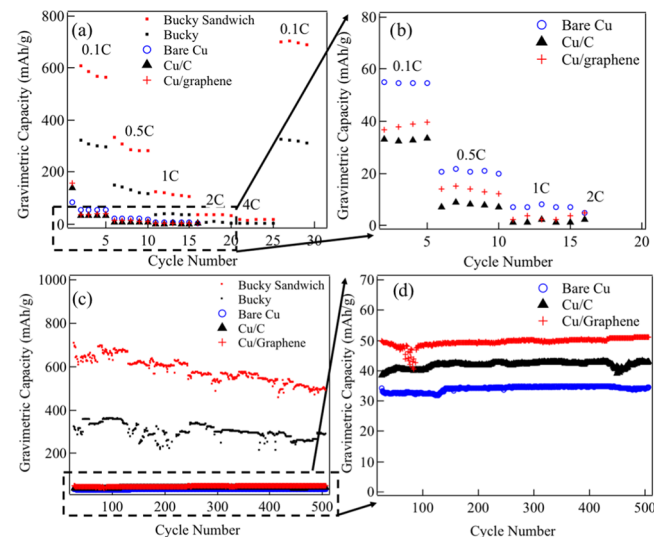


Figure 4. (a) Rate capability tests of coin cells made of electrodes used in this study, (b) a magnified view of the data shown in the box in (a), (c) cyclability of electrodes used in this study at a 0.1 C rate, and (d) a magnified view of the cyclability of Cu-based electrodes.

addition, we provide the volumetric capacity of the samples discussed above in Figure S7.

It is interesting to note that the Cu/C and Cu/graphene electrodes showed much lower capacity (~ 40 and 50 mAh/g at 0.1 C after 25 cycles, respectively) compared to Bucky and Bucky sandwich electrodes (~ 380 and ~ 620 mAh/g after 25 cycles, respectively) although their R_{ct} values were an order of magnitude lower than bare Cu electrodes (cf. Figure 3 and Table 1). Thus, the superior performance of Bucky and Bucky sandwich cannot be attributed only to a decrease in the charge-transfer resistance between the bottom-most AM layer and Cu foil. Another important factor that contributes to the improved performance of Bucky and Bucky sandwich electrodes is their ability to facilitate a three-dimensional electrically connected network that lowers the CCAMI over the entire AM layer (which addresses challenge 1 discussed in the Introduction section). Although Si NPs < 150 nm mitigate pulverization effects, their volume expansion upon lithiation leads to fused Si NPs with larger diameter. In the case of our electrodes, the Si NP average diameter increases from < 100 nm to a few microns within 10 cycles (Figure 5a–c). Such fusion of Si NPs leads to large cracks in the AM layer that in turn result (see Figure 2) in

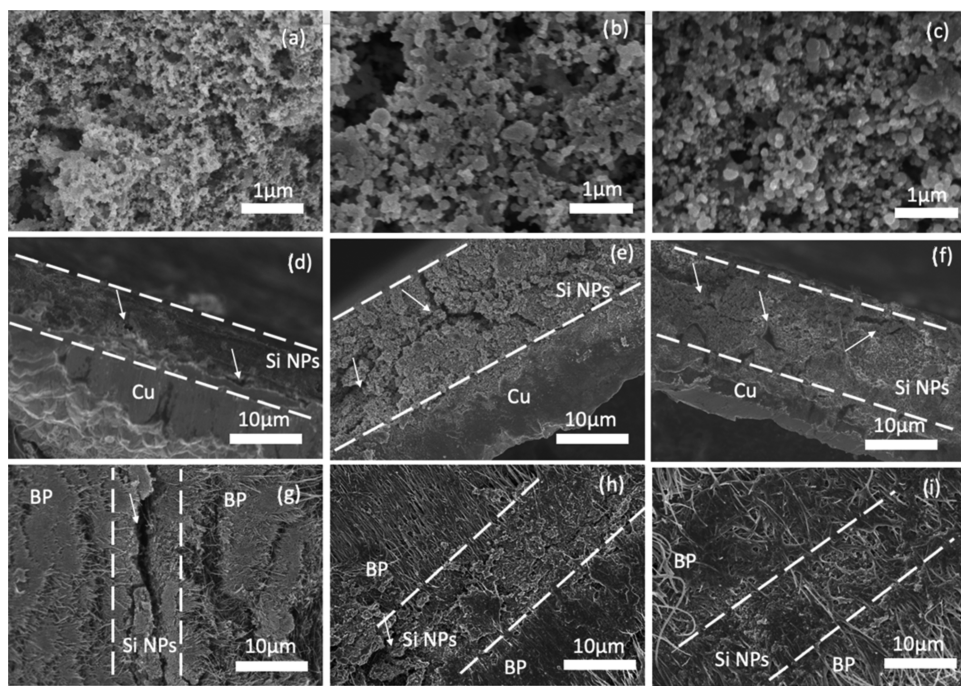


Figure 5. Scanning electron micrographs showing a top view of Si NPs on Cu electrodes after (a) 0, (b) 10, and (c) 100 cycles. Cross-sectional scanning electron micrographs of the Cu electrode after (d) 0, (e) 10, and (f) 100 cycles. The cracks within the AM layer are highlighted using white arrows. In the case of Bucky sandwich (g) electrodes, the tubular nature of CNTs allows them to envelop Si NPs providing a percolating electrical path even in the presence of large cracks. Even after (h) 10 and (i) 100 cycles, the tubular nature of CNTs is still retained.

Table 1. Charge-Transfer Resistance, Warburg Coefficients, and Diffusion Time Constants Derived by Fitting EIS Data

sample name	R_{ct} (Ω) (25th cycle)	Warburg coefficient ($\Omega/s^{1/2}$)	$\frac{\tau_D}{\tau_D \text{bare Cu}}$
bare Cu	643	232	1
Cu/C	58	23	9.7
Cu/graphene	73	15	15.11
Bucky	25	4	55.6
Bucky sandwich	21	1.5	150.5

complete electrical disconnection of many regions from the CC even if the AM layer is not mechanically delaminated. For instance, our detailed cross-sectional SEM images of electrodes after cycling showed that significant cracks develop within AM layers for Cu-based electrodes over only 10 cycles (Figure 5d–f). In the case of Bucky and Bucky sandwich structures, we found that the CNTs act as interdigitated electrical connections even over many cycles (see Figure 5g–i). Indeed, as seen in Figure 5g–i, such interdigitated CNT connections in Bucky and Bucky sandwich electrodes allow them to withstand high rates up to 4 C unlike Cu-based electrodes (cf. Figure 4a). In addition to SEM images in Figure 5, cross-sectional and top-view elemental maps for C, Si, Fe (which is present as a catalyst particle inside CNTs in BPs), and Cu for all electrodes after 0, 10, and 100 cycles are shown in Figures 6 and 7.

Although cross-sectional images of Bucky and Bucky sandwich (see Figure 6) showed no delamination, their top-view images (Figure 7) showed the presence of cracks within the Si NP layer. Nonetheless, as shown in Figure 7f, we found that CNTs (appearing green due to the presence of the Fe catalyst) in BP/Si NP electrodes provide conducting channels through the cracks unlike the Cu/Si NP electrode (cf. Figure 2). Finally, as shown in Figure 8, we also obtained cross-

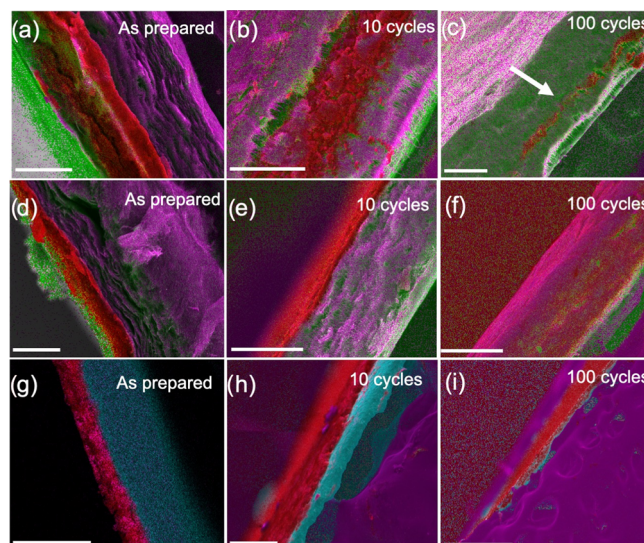


Figure 6. Cross-sectional elemental maps for (a–c) BP/Si NPs/BP, (d–f) BP/Si NPs, and (g–i) Cu/Si NPs at different stages (as prepared, 10 cycles, and 100 cycles) show that the layer of Si NPs does not delaminate from the electrodes upon cycling. As shown by the white arrow in panel (c), Si NPs are still sandwiched between BPs even after 100 cycles. Different colors correspond to different elements (magenta for C, red for Si, blue for Cu, and green for Fe). It should be noted that Fe catalyst particles embedded in CNTs appear in BP/Si NPs and BP/Si NPs/BP electrodes. All of the scale bars are 100 μ m.

sectional images of the BP/Si NP/BP electrode. Clearly, we were able to find Si NPs sandwiched between BPs even after 100 cycles (cf. Figure 8h) concurring with low charge-transfer (cf. Figure 3) impedance and superior electrochemical performance of BP-based electrodes.

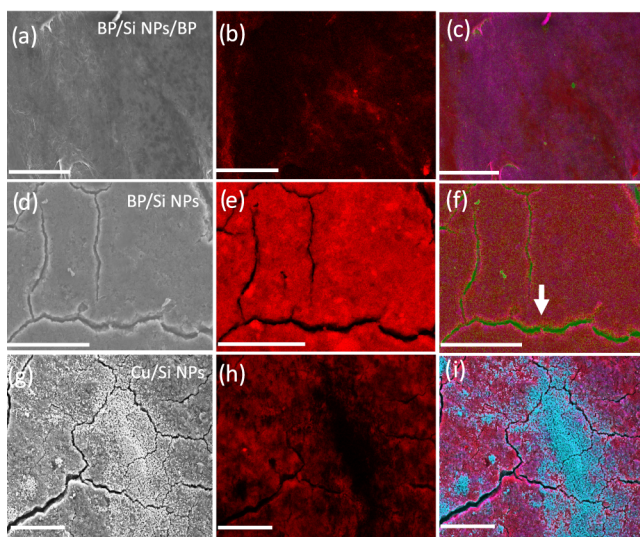


Figure 7. Top view of electrodes and corresponding elemental maps for (a–c) BP/Si NPs/BP, (d–f) BP/Si NPs, and (g–i) Cu/Si NPs after 100 cycles. As shown by the white arrow in panel (f), CNTs in BP provide electrical contact through the cracks unlike Cu/Si NPs. Different colors correspond to different elements (magenta for C, red for Si, blue for Cu, and green for Fe). The top view of BP/Si NPs/BP (panel a) shows the surface of BP instead of Si NPs as Si NPs are sandwiched below the top BP layer. It should be noted that Fe catalyst particles embedded in CNTs appear in BP/Si NPs and BP/Si NPs/BP electrodes. All of the scale bars are 100 μ m.

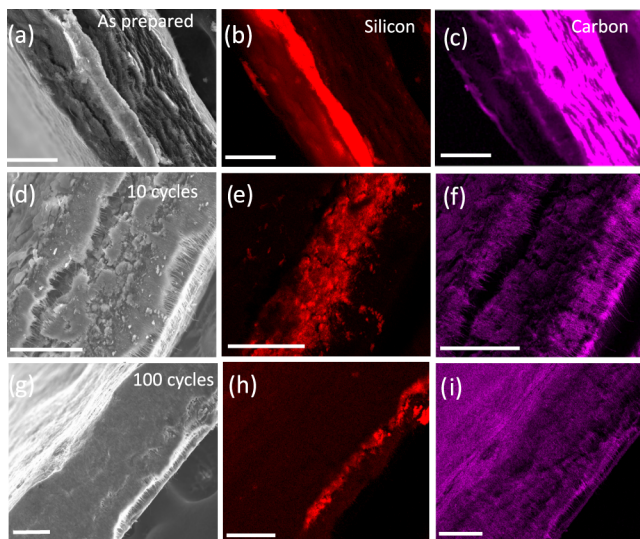


Figure 8. Cross-sectional electron micrographs and corresponding elemental maps (Si and C) of BP/Si NP/BP electrodes after (a–c) 0, (d–f) 10, and (g–i) 100 cycles. All of the scale bars are 100 nm.

Returning to Figure 3, it can be seen that Bucky and Bucky sandwich electrodes facilitate fast diffusion of Li^+ . In the case of bare Cu, Cu/C, and Cu/graphene electrodes, the frequency region of the EIS spectrum (<10 Hz) shows a clear semi-infinite diffusion element (observed as a line following the semicircle in Figure 3) due to the presence of the metallic current collector interface. In the case of semi-infinite diffusion, the Warburg impedance Z_W can be expressed in the complex plane as³⁵

$$Z_W = \sigma(1 - j)\omega^{-1/2} \quad (1)$$

In the above equation, σ is the Warburg coefficient and ω is the frequency. As shown in Figure 9 and Table 1, we found

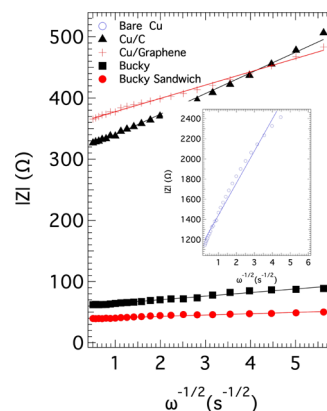


Figure 9. Impedance is plotted as a function of the inverse square root of frequency for obtaining the Warburg coefficients from the slope. The data for bare Cu in the inset figure is similar.

that the Warburg coefficients (obtained from fitting $|Z_W|$ vs $\omega^{-1/2}$) for Bucky and Bucky sandwich electrodes are significantly low compared to those for bare Cu, Cu/C, and Cu/graphene. Such a difference could be attributed to the ability of Li^+ ions to diffuse into BP and facilitate fast diffusion through a quasi-3D network of CNTs. As discussed in refs 35, 36, the Warburg coefficient is directly proportional to the diffusion time constant for Li (τ_D)

$$\sigma = \frac{Q_f M_w}{nFC} \sqrt{\frac{\tau_D}{2}} \quad (2)$$

In eq 2, Q_f is the specific capacity, M_w is the molecular weight, F is the Faraday constant, and n is the charge-transfer number of lithium. The Warburg coefficient for Bucky sandwich electrodes was at least 2 orders of magnitude smaller compared to that for bare Cu (see Table 1). Although Cu/C and Cu/graphene significantly reduced the charge-transfer resistance, their Warburg coefficients are an order of magnitude higher than Bucky and Bucky sandwich electrodes (see Table 1). Using eq 2, the diffusion time constant for Bucky sandwich (/Bucky) electrode is 150 times (/55 times) lower than those for bare Cu electrodes. This suggests that CNTs in BPs significantly reduce the diffusion constant and thus increase the capacity (see Table 1).

Given the observed improvement in the case of 100 nm Si NPs (as discussed in Figures 1–9), we prepared Bucky sandwich electrodes using ~30 nm Si NPs with a significantly higher surface area (~257 m^2/g). As expected, we observed a significant increase in the gravimetric capacity compared to Cu-based electrodes. Indeed, as shown in Figure 10, we found that Bucky sandwich with high-surface-area Si NPs leads to capacities as high as 1635 mAh/g at 0.1 C when discharged between 0.01–0.1 V and ~1490 mAh/g at 0.1 C for 0.1–1 V window. Furthermore, we found that the electrodes were highly stable up to 100 cycles. Finally, a table comparing the capacity of the Bucky sandwich electrode with other electrodes of similar mass density is presented in Table S2.

CONCLUSIONS

In summary, we demonstrated that Bucky sandwich electrodes simultaneously mitigate diffusion impedance in addition to the

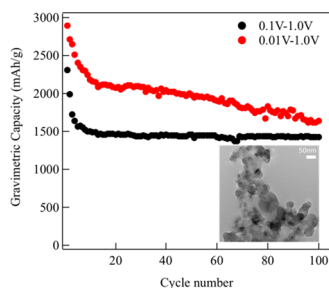


Figure 10. Cyclability of the Bucky sandwich electrodes tested at 0.1 C for 30 nm diameter Si NPs in two different voltage ranges: 0.1–1 V and 0.01–1 V. The inset is the TEM image of the as-purchased Si NPs of diameter \sim 30 nm.

large charge-transfer impedance. The Bucky sandwich electrodes with Si NPs (diameter \sim 30 nm) exhibited a capacity as high as \sim 1635 mAh/g (\sim 1490 mAh/g) while discharged to 0.01 V (0.1 V) after 100 cycles. Furthermore, (i) these Bucky electrodes were able to withstand a high C rate of 4 C, where traditional electrodes containing Si NPs fail, (ii) our extensive EIS studies revealed that the Li-ion diffusion time constant is \sim 150 times smaller than that of traditional Cu-based electrodes.

EXPERIMENTAL DETAILS

Materials and Electrode Preparation. Electrode slurry was prepared by mixing Si NPs (100 nm from MTI Corp; 30 nm from ACS materials), poly(vinylidene fluoride) (PVDF, Sigma-Aldrich), and TIMICAL Graphite and Carbon super P (MTI Corp) with a mass ratio of 6:2:2 in *N*-methyl-2-pyrrolidone (NMP, Sigma-Aldrich). First, PVDF was dissolved in NMP at 80 °C, and then a mixture of the Si NPs and Super P was added at room temperature. The slurry was stirred for 12 h to form a viscous homogeneous mixture. It was coated on Cu foil (MTI Corp), carbon-coated Cu foil (MTI Corp), 3–5 layer graphene-coated Cu foil (ACS material), and a 60 GSM Bucky paper (Nanotech Lab) using an adjustable doctor blade. The coated samples were dried for 12 h at room temperature and another 12 h at 100 °C in a precision compact oven. Working electrodes of diameter 10 mm were punched. The Brunauer–Emmett–Teller (BET) surface area of 100 nm Si was found to be \sim 80 m²/g and 30 nm Si was \sim 257 m²/g. For the Bucky sandwich electrode, another Bucky (same diameter as that for the working electrode) was punched and pressed together with the working electrode.

Material and Electrochemical Characterization. Scanning electron microscopy and elemental map images were obtained using a Hitachi SEM-4800. CR2032-type coin cells were assembled using a working electrode and a Li chip (15.6 nm diameter \times 0.45 mm thickness, MTI Corp) as the counter electrode, inside the glove box. For the electrolyte, we used 1 M lithium hexafluorophosphate (LiPF₆) in ethylene carbonate and dimethyl carbonate (v/v = 1:1, Sigma-Aldrich). Celgard 2325 (Celgard, LLC) was used as the separator. The galvanostatic charge/discharge was performed using an MTI battery analyzer system in the voltage range of 0.1–1.0 V unless specified otherwise (for example, during deep discharge). First, the rate capability test was performed at different C-rates (0.1, 0.5, 1, 2, and 4 C), and then, cycling stability was performed for only 0.1 C rate (1 C = 4200 mA/g) for all batteries. Electrochemical impedance spectroscopy (EIS) was carried out from 1 MHz to 0.1 Hz at 0.1 V by applying an ac amplitude of 10 mV. EIS data were fitted using Gamry Echem analyst software.

ASSOCIATED CONTENT

Supporting Information

The Supporting Information is available free of charge at <https://pubs.acs.org/doi/10.1021/acsami.0c05888>.

A detailed EIS data; BP morphology; irreversible discharge data; volumetric capacity data; and a table comparing the Bucky sandwich performance with other electrodes in the literature ([PDF](#))

AUTHOR INFORMATION

Corresponding Author

Ramakrishna Podila — Department of Physics and Astronomy, Clemson Nanomaterials Institute, Anderson, South Carolina 29625, United States; Laboratory of Nano-Biophysics, Clemson University, Clemson, South Carolina 29634, United States; Email: rpodila@g.clemson.edu

Authors

Shailendra Chiluwal — Department of Physics and Astronomy, Clemson Nanomaterials Institute, Anderson, South Carolina 29625, United States; Laboratory of Nano-Biophysics, Clemson University, Clemson, South Carolina 29634, United States; [ORCID](#) [0000-0003-3556-2938](https://orcid.org/0000-0003-3556-2938)

Nawraj Sapkota — Department of Physics and Astronomy, Clemson Nanomaterials Institute, Anderson, South Carolina 29625, United States

Apparao M. Rao — Department of Physics and Astronomy, Clemson Nanomaterials Institute, Anderson, South Carolina 29625, United States; [ORCID](#) [0000-0002-1450-3499](https://orcid.org/0000-0002-1450-3499)

Complete contact information is available at: <https://pubs.acs.org/10.1021/acsami.0c05888>

Notes

The authors declare no competing financial interest.

ACKNOWLEDGMENTS

This work was financially supported by NASA-EPSCoR award under #NNH17ZHA002C, South Carolina EPSCoR/IDeA Program under Award #18-SR03, South Carolina GEAR MADE IN SC award (19-GE-01), and Clemson University Core Incentivized Access R-Initiative grant.

REFERENCES

- (1) Liu, Y.; Zhu, Y.; Cui, Y. Challenges and Opportunities towards Fast-Charging Battery Materials. *Nat. Energy* **2019**, *4*, 540–550.
- (2) Goriparti, S.; Miele, E.; De Angelis, F.; Di Fabrizio, E.; Zaccaria, R. P.; Capiglia, C. Review on Recent Progress of Nanostructured Anode Materials for Li-Ion Batteries. *J. Power Sources* **2014**, *257*, 421–443.
- (3) Wagemaker, M.; Mulder, F. M. Properties and Promises of Nanosized Insertion Materials for Li-Ion Batteries. *Acc. Chem. Res.* **2013**, *46*, 1206–1215.
- (4) Moretti, A.; Kim, G.-T.; Bresser, D.; Renger, K.; Paillard, E.; Marassi, R.; Winter, M.; Passerini, S. Investigation of Different Binding Agents for Nanocrystalline Anatase TiO₂ Anodes and Its Application in a Novel, Green Lithium-Ion Battery. *J. Power Sources* **2013**, *221*, 419–426.
- (5) Hong, Z.; Wei, M. Layered Titanate Nanostructures and Their Derivatives as Negative Electrode Materials for Lithium-Ion Batteries. *J. Mater. Chem. A* **2013**, *1*, 4403.
- (6) Chen, Z.; Belharouak, I.; Sun, Y.-K.; Amine, K. Titanium-Based Anode Materials for Safe Lithium-Ion Batteries. *Adv. Funct. Mater.* **2013**, *23*, 959–969.
- (7) Zhu, B.; Wang, X.; Yao, P.; Li, J.; Zhu, J. Towards High Energy Density Lithium Battery Anodes: Silicon and Lithium. *Chem. Sci.* **2019**, *10*, 7132–7148.
- (8) Wu, H.; Cui, Y. Designing Nanostructured Si Anodes for High Energy Lithium Ion Batteries. *Nano Today* **2012**, *7*, 414–429.

(9) Szczech, J. R.; Jin, S. Nanostructured Silicon for High Capacity Lithium Battery Anodes. *Energy Environ. Sci.* **2011**, *4*, 56–72.

(10) Zuo, X.; Zhu, J.; Müller-Buschbaum, P.; Cheng, Y.-J. Silicon Based Lithium-Ion Battery Anodes: A Chronicle Perspective Review. *Nano Energy* **2017**, *31*, 113–143.

(11) Ma, D.; Cao, Z.; Hu, A. Si-Based Anode Materials for Li-Ion Batteries: A Mini Review. *Nano-Micro Lett.* **2014**, *6*, 347–358.

(12) Sun, Y.; Liu, N.; Cui, Y. Promises and Challenges of Nanomaterials for Lithium-Based Rechargeable Batteries. *Nat. Energy* **2016**, *1*, No. 16071.

(13) Kalnajs, S.; Rhodes, K.; Daniel, C. A Study of Lithium Ion Intercalation Induced Fracture of Silicon Particles Used as Anode Material in Li-Ion Battery. *J. Power Sources* **2011**, *196*, 8116–8124.

(14) Lee, S. W.; McDowell, M. T.; Berla, L. A.; Nix, W. D.; Cui, Y. Fracture of Crystalline Silicon Nanopillars during Electrochemical Lithium Insertion. *Proc. Natl. Acad. Sci. U.S.A.* **2012**, *109*, 4080–4085.

(15) McDowell, M. T.; Ryu, I.; Lee, S. W.; Wang, C.; Nix, W. D.; Cui, Y. Studying the Kinetics of Crystalline Silicon Nanoparticle Lithiation with In Situ Transmission Electron Microscopy. *Adv. Mater.* **2012**, *24*, 6034–6041.

(16) Liu, X. H.; Zhong, L.; Huang, S.; Mao, S. X.; Zhu, T.; Huang, J. Y. Size-Dependent Fracture of Silicon Nanoparticles during Lithiation. *ACS Nano* **2012**, *6*, 1522–1531.

(17) Aghajamali, M.; Xie, H.; Javadi, M.; Kalisvaart, W. P.; Buriak, J. M.; Veinot, J. G. C. Size and Surface Effects of Silicon Nanocrystals in Graphene Aerogel Composite Anodes for Lithium Ion Batteries. *Chem. Mater.* **2018**, *30*, 7782–7792.

(18) Luo, J.; Zhao, X.; Wu, J.; Jang, H. D.; Kung, H. H.; Huang, J. Crumpled Graphene-Encapsulated Si Nanoparticles for Lithium Ion Battery Anodes. *J. Phys. Chem. Lett.* **2012**, *3*, 1824–1829.

(19) Lee, J. K.; Smith, K. B.; Hayner, C. M.; Kung, H. H. Silicon Nanoparticles–Graphene Paper Composites for Li Ion Battery Anodes. *Chem. Commun.* **2010**, *46*, 2025–2027.

(20) Zhou, X.; Yin, Y.-X.; Wan, L.-J.; Guo, Y.-G. Facile Synthesis of Silicon Nanoparticles Inserted into Graphene Sheets as Improved Anode Materials for Lithium-Ion Batteries. *Chem. Commun.* **2012**, *48*, 2198–2200.

(21) Zhou, X.; Yin, Y.-X.; Wan, L.-J.; Guo, Y.-G. Self-Assembled Nanocomposite of Silicon Nanoparticles Encapsulated in Graphene through Electrostatic Attraction for Lithium-Ion Batteries. *Adv. Energy Mater.* **2012**, *2*, 1086–1090.

(22) Chang, J.; Huang, X.; Zhou, G.; Cui, S.; Hallac, P. B.; Jiang, J.; Hurley, P. T.; Chen, J. Multilayered Si Nanoparticle/Reduced Graphene Oxide Hybrid as a High-Performance Lithium-Ion Battery Anode. *Adv. Mater.* **2014**, *26*, 758–764.

(23) Wu, H.; Yu, G.; Pan, L.; Liu, N.; McDowell, M. T.; Bao, Z.; Cui, Y. Stable Li-Ion Battery Anodes by in-Situ Polymerization of Conducting Hydrogel to Conformally Coat Silicon Nanoparticles. *Nat. Commun.* **2013**, *4*, No. 1943.

(24) Li, G.; Huang, L. B.; Yan, M. Y.; Li, J. Y.; Jiang, K. C.; Yin, Y. X.; Xin, S.; Xu, Q.; Guo, Y. G. An Integral Interface with Dynamically Stable Evolution on Micron-Sized SiO_x Particle Anode. *Nano Energy* **2020**, *74*, No. 104890.

(25) Ventrapragada, L. K.; Zhu, J.; Creager, S. E.; Rao, A. M.; Podila, R. A Versatile Carbon Nanotube-Based Scalable Approach for Improving Interfaces in Li-Ion Battery Electrodes. *ACS Omega* **2018**, *3*, 4502–4508.

(26) Ventrapragada, L. K.; Creager, S. E.; Rao, A. M.; Podila, R. Carbon Nanotubes Coated Paper as Current Collectors for Secondary Li-Ion Batteries. *Nanotechnol. Rev.* **2019**, *8*, 18–23.

(27) Kim, H. R.; Choi, W. M. Graphene Modified Copper Current Collector for Enhanced Electrochemical Performance of Li-Ion Battery. *Scr. Mater.* **2018**, *146*, 100–104.

(28) Dsoke, S.; Tian, X.; Täubert, C.; Schlüter, S.; Wohlfahrt-Mehrens, M. Strategies to Reduce the Resistance Sources on Electrochemical Double Layer Capacitor Electrodes. *J. Power Sources* **2013**, *238*, 422–429.

(29) Yuan, L.-X.; Wang, Z.-H.; Zhang, W.-X.; Hu, X.-L.; Chen, J.-T.; Huang, Y.-H.; Goodenough, J. B. Development and Challenges of LiFePO₄ Cathode Material for Lithium-Ion Batteries. *Energy Environ. Sci.* **2011**, *4*, 269.

(30) Yoshihara, S.; Katsuta, H.; Isozumi, H.; Kasai, M.; Oyaizu, K.; Nishide, H. Designing Current Collector/Composite Electrode Interfacial Structure of Organic Radical Battery. *J. Power Sources* **2011**, *196*, 7806–7811.

(31) Wu, H. C.; Lee, E.; Wu, N. L.; Jow, T. R. Effects of Current Collectors on Power Performance of Li₄Ti₅O₁₂ Anode for Li-Ion Battery. *J. Power Sources* **2012**, *197*, 301–304.

(32) Wu, H. C.; Wu, H. C.; Lee, E.; Wu, N. L. High-Temperature Carbon-Coated Aluminum Current Collector for Enhanced Power Performance of LiFePO₄ Electrode of Li-Ion Batteries. *Electrochim. Commun.* **2010**, *12*, 488–491.

(33) Xia, F.; Kwon, S.; Lee, W. W.; Liu, Z.; Kim, S.; Song, T.; Choi, K. J.; Paik, U.; Park, W. I. Graphene as an Interfacial Layer for Improving Cycling Performance of Si Nanowires in Lithium-Ion Batteries. *Nano Lett.* **2015**, *15*, 6658–6664.

(34) Orazem, M. E.; Tribollet, B. Constant-Phase Elements. In *Electrochemical Impedance Spectroscopy*; John Wiley & Sons, Inc.: Hoboken, NJ, 2017; pp 395–419.

(35) Ho, C.; Raistrick, I. D.; Huggins, R. A. Application of A-C Techniques to the Study of Lithium Diffusion in Tungsten Trioxide Thin Films. *J. Electrochem. Soc.* **1980**, *127*, 343–350.

(36) Mohamedi, M.; Makino, M.; Dokko, K.; Itoh, T.; Uchida, I. Electrochemical Investigation of LiNi_{0.5}Mn_{1.5}O₄ Thin Film Intercalation Electrodes. *Electrochim. Acta* **2002**, *48*, 79–84.